

A TWO-DIMENSIONAL ALFVÉN-WAVE-DRIVEN SOLAR WIND MODEL

Y. CHEN and Y. Q. HU

Department of Earth and Space Sciences, University of Science and Technology of China, Hefei, Anhui 230026, China

(Received 1 November 2000; accepted 29 November 2000)

Abstract. This paper presents a two-dimensional, Alfvén-wave-driven solar wind model, in which the wave energy is assumed to cascade from the low-frequency Alfvén waves to high-frequency ion cyclotron waves and to be transferred to the solar wind protons by cyclotron resonance at the Kolmogorov rate. A typical structure in the meridional plane consisting of a coronal streamer near the Sun, a fast wind in high latitudes, and a slow wind across the heliospheric current sheet, is found. The fast wind obtained in the polar region is essentially similar to that derived by previous one-dimensional flow-tube models, and its density profile in the vicinity of the Sun roughly matches relevant observations. The proton conditions at 1 AU are also consistent with observations for both the fast and slow winds. The Alfvén waves appear in the fast- and slow-wind regions simultaneously and have comparable amplitudes, which agrees with *Helios* observations. The acceleration and heating of the solar wind by the Alfvén waves are found to occur mainly in the near-Sun region. It is demonstrated in terms of one-dimensional calculations that the distinct properties of the fast and slow winds are mainly attributed to different geometries of the flow tubes associated with the two sorts of winds. In addition, the 2-D and 1-D simulations give essentially the same results for both the fast and the slow winds.

1. Introduction

As a decisive factor of the interplanetary dynamical processes, the solar wind has since its discovery aroused extensive interest in the community of solar-terrestrial physics. However, it remains open how the solar wind is accelerated and heated. Most previous studies were concentrated on the fast solar wind, and purely thermal driving was found to fail to produce the observational features, so a non-thermal mechanism is needed to accelerate and heat the fast solar wind. Presently, the cascade and dissipation of Alfvén waves proposed by Tu, Pu, and Wei (1984) seem to be a plausible and well-considered non-thermal mechanism and were used to explain the extensive heating of the solar wind and the radial evolution of the Alfvénic fluctuation spectrum (Tu, 1987, 1988; Hu, Habbal, and Li, 1999). Recently, such a mechanism was applied to the preferential acceleration and heating of the heavy ions near the Sun (Hu and Habbal, 1999; Hu, Esser, and Habbal, 2000). These studies were still limited to one-dimensional flow tubes and the fast solar wind. However, Alfvén waves were also observed in the slow solar wind (Marsch *et al.*, 1981; Roberts, 1987), and this raises a question why the slow



wind is not as efficiently accelerated and heated as the fast wind is. To answer this question, it is necessary to include the two winds into a unified model and to carry out multi-dimensional simulations.

Multi-dimensional models for the corona appeared as early as 1970s (e.g., Pneuman and Kopp, 1971; Steinolfson, Suess, and Wu, 1982). Most of such studies were aimed at creating a background solar corona for analyzing the propagation and evolution of solar disturbances. They treated the energy equation in various approximate ways, either using the polytropic process with a polytropic index less than the adiabatic value so as to represent the additional heating of the solar wind (e.g., Wang *et al.*, 1993), or introducing artificial acceleration and heating in the corona (e.g., Suess *et al.*, 1999; Suess, Wang, and Wu, 1996) which is commonly adopted in earlier flow-tube models. To our knowledge, Usmanov *et al.* (2000) were the first to incorporate the acceleration and heating effects of Alfvén waves in a multi-dimensional model, and to successfully reproduce the *Ulysses* observations during its first latitude traversal in 1994–1995. They illustrated the importance of the Alfvén waves in generating a fast solar wind at high latitudes. However, the polytropic index in their model was set to be less than the adiabatic value $\frac{5}{3}$, implying an extraneous heating source in addition to the wave heating. Moreover, the Alfvén-wave pressure obtained vanishes in the equatorial plane, and rapidly increases across a narrow latitudinal transition layer less than 10° in width to a normal value in the fast wind region, which is inconsistent with the *Helios* observations. Finally, the dissipation rate was assumed to be proportional to the wave pressure with a damping length as a function of the heliocentric distance. Such a choice is somewhat artificial.

Based on the work by Usmanov *et al.* (2000) the present study makes the following improvements: (1) to adopt the Alfvén waves as the unique energy source by taking the adiabatic value for the polytropic index ($\gamma = \frac{5}{3}$), and (2) to use the Kolmogorov rate (Hollweg, 1986) as the dissipation rate for the Alfvén waves, which is physically more plausible. Our emphasis is placed on elucidating why the Alfvén waves display distinct acceleration and heating effects in the fast and slow winds while they exist in both winds and have comparable amplitudes. The physical model and initial-boundary conditions are addressed in Section 2, and the numerical results are discussed in Section 3. Concluding remarks are given in Section 4.

2. Physical Model and Initial-Boundary Conditions

For axisymmetric problems in the spherical coordinates (r, θ, ϕ) , a magnetic flux function $\psi(r, \theta)$ is introduced and related to the magnetic field by

$$\mathbf{B} = \nabla \psi \frac{\hat{\phi}}{r \sin \theta}, \quad (1)$$

and then the two-dimensional MHD equations in the meridional plane may be cast into the following form:

$$\frac{\partial \rho}{\partial t} + \rho \frac{\partial v_r}{\partial r} + v_r \frac{\partial \rho}{\partial r} + \frac{2\rho v_r}{r} + \frac{\rho v_\theta \cot \theta}{r} + \frac{v_\theta \partial \rho}{r \partial \theta} + \frac{\rho \partial v_\theta}{r \partial \theta} = 0, \tag{2}$$

$$\begin{aligned} \frac{\partial v_r}{\partial t} + v_r \frac{\partial v_r}{\partial r} + \frac{v_\theta \partial v_r}{r \partial \theta} + \frac{R(T_e + T_p)}{\rho} \frac{\partial \rho}{\partial r} + \frac{R \partial(T_e + T_p)}{\partial r} + \\ + \frac{L\psi}{\mu_0 \rho} \frac{\partial \psi}{\partial r} + \frac{1}{\rho} \frac{\partial p_w}{\partial r} - \frac{v_\theta^2}{r} + \frac{GM}{r^2} = 0, \end{aligned} \tag{3}$$

$$\begin{aligned} \frac{\partial v_\theta}{\partial t} + v_r \frac{\partial v_\theta}{\partial r} + \frac{v_\theta \partial v_\theta}{r \partial \theta} + \frac{R(T_e + T_p)}{\rho r} \frac{\partial \rho}{\partial \theta} + \frac{R \partial(T_e + T_p)}{r \partial \theta} + \\ + \frac{L\psi}{\mu_0 \rho r} \frac{\partial \psi}{\partial \theta} + \frac{1}{\rho r} \frac{\partial p_w}{\partial \theta} + \frac{v_r v_\theta}{r} = 0, \end{aligned} \tag{4}$$

$$\frac{\partial \psi}{\partial t} + v_r \frac{\partial \psi}{\partial r} + \frac{v_\theta \partial \psi}{r \partial \theta} = 0, \tag{5}$$

$$\begin{aligned} \frac{\partial T_e}{\partial t} + v_r \frac{\partial T_e}{\partial r} + \frac{v_\theta \partial T_e}{r \partial \theta} + (\gamma - 1)T_e \frac{\partial v_r}{\partial r} + \frac{(\gamma - 1)T_e \partial v_\theta}{r \partial \theta} + \frac{2(\gamma - 1)T_e v_r}{r} + \\ + \frac{(\gamma - 1)T_e v_\theta \cot \theta}{r} + v_E(T_e - T_p) - \frac{\gamma - 1}{\rho R} \nabla(\kappa_e \nabla T_e) = 0, \end{aligned} \tag{6}$$

$$\begin{aligned} \frac{\partial T_p}{\partial t} + v_r \frac{\partial T_p}{\partial r} + \frac{v_\theta \partial T_p}{r \partial \theta} + (\gamma - 1)T_p \frac{\partial v_r}{\partial r} + \frac{(\gamma - 1)T_p \partial v_\theta}{r \partial \theta} + \frac{2(\gamma - 1)T_p v_r}{r} + \\ + \frac{(\gamma - 1)T_p v_\theta \cot \theta}{r} + v_E(T_p - T_e) - \frac{\gamma - 1}{nk} Q = 0, \end{aligned} \tag{7}$$

$$\begin{aligned} \frac{\partial p_w}{\partial t} + v_r \frac{\partial p_w}{\partial r} + \frac{v_\theta \partial p_w}{r \partial \theta} + \frac{1}{\sqrt{\mu_0 \rho} r^2 \sin \theta} \left(\frac{\partial p_w}{\partial r} \frac{\partial \psi}{\partial \theta} - \frac{\partial p_w}{\partial \theta} \frac{\partial \psi}{\partial r} \right) + \\ + \frac{3p_w}{2} \frac{\partial v_r}{\partial r} + \frac{3p_w}{2r} \frac{\partial v_\theta}{\partial \theta} - \frac{p_w}{2r^2 \sin \theta \sqrt{\mu_0 \rho}} \left(\frac{\partial \rho}{\partial r} \frac{\partial \psi}{\partial \theta} - \frac{\partial \rho}{\partial \theta} \frac{\partial \psi}{\partial r} \right) + \\ + \frac{3v_r p_w}{r} + \frac{3v_\theta p_w}{2r} \cot \theta + \frac{Q}{2} = 0, \end{aligned} \tag{8}$$

where

$$L\psi = \frac{1}{r^2 \sin^2 \theta} \left(\frac{\partial^2 \psi}{\partial r^2} + \frac{1}{r^2} \frac{\partial^2 \psi}{\partial \theta^2} - \frac{\cot \theta}{r^2} \frac{\partial \psi}{\partial \theta} \right),$$

ρ ($= nm_p$) is the plasma density, v_r and v_θ the flow velocity components, T_e and T_p the electron and proton temperatures, $p_w = \rho \langle \delta v^2 \rangle / 2$ the Alfvén wave pressure, M , G , k and γ are the Sun's mass, the gravitational constant, the Boltzmann constant, and the adiabatic index ($\gamma = 5/3$) respectively, and ν_E the electron-proton collision frequency taken to be $9.094 \times 10^{-8} n T_e^{-3/2}$ (Braginskii, 1965). Following Hu, Habbal, and Li (1997), we use the classical thermal conductivity for electrons (Spitzer, 1962) and ignore the proton thermal conduction.

The cascade and dissipation of the Alfvén waves depend on the wave spectrum. A rigorous way to address this is to simultaneously solve the wave spectrum equation and the solar wind flow equations (Tu, 1987; Hu, Habbal, and Li, 1999). In order to avoid the complexity associated with the solution of the wave spectrum equation, we follow the approach proposed by Hollweg (1986), namely, we start from the wave pressure Equation (8) in terms of a prescribed dissipation rate Q . There are generally two choices for Q , the Kolmogorov rate (Hollweg, 1986) and the Kraichnan rate (Hollweg and Johnson, 1988), expressed by

$$Q_{\text{kol}} = \rho \langle \delta v^2 \rangle^{3/2} / L_c \quad (9)$$

and

$$Q_{\text{kra}} = \rho \langle \delta v^2 \rangle^2 / (L_c v_A), \quad (10)$$

respectively, where $\langle \delta v^2 \rangle$ is the velocity variance associated with the wave field, L_c is the correlation length of the fluctuations given by $L_c = L_{c0} (B_c / B)^{1/2}$ (B_c is the magnetic field strength at the coronal base), and v_A is the Alfvén wave speed. Hu, Habbal, and Li (1999, referred to as Paper HHL hereinafter) used a one-dimensional flow tube model and solved the Alfvén wave spectrum equation and the solar wind flow equations simultaneously so as to consistently obtain the dissipation rate Q . They compared Q with Q_{kol} and Q_{kra} obtained from Equations (9) and (10) respectively, and found that Q_{kol} is closer to Q . Therefore, we will use Equation (9) for the dissipation rate, and set $L_{c0} = 7.7 \times 10^4$ km and $B_c = B_{c0}$ for simplicity, where B_{c0} is the magnetic field strength at the polar coronal base.

The computational domain is taken to be $1R_s \leq r \leq 1$ AU, $0^\circ \leq \theta \leq 90^\circ$, divided into two sub-domains along the radial direction: $1R_s \leq r \leq 10R_s$ (sub-domain I) and $10R_s \leq r \leq 1$ AU (sub-domain II). A 50×40 mesh is laid out for both sub-domains. The grid spacing in the radial direction increases in terms of geometric series from $0.03R_s$ at the coronal base to $0.8R_s$ at $10R_s$ with a common ratio 1.076 for sub-domain I and from $1.0R_s$ at $10R_s$ to $10.9R_s$ at 1 AU with a common ratio 1.05 for sub-domain II. The grid spacing in the θ direction increases from 0.5° at the equator to 6.8° at the polar axis in terms of a geometric series of common ratio 1.073 for both sub-domains with $\theta_2 = -\theta_1 = 3.4^\circ$, $\theta_{38} = 89.5^\circ$, $\theta_{39} = 90^\circ$, and $\theta_{40} = 90.5^\circ$. In the practical calculations, the top of sub-domain I was extended to $15R_s$ so as to reduce the numerical errors associated with the boundary conditions there. The grid spacing is slightly too large to properly resolve

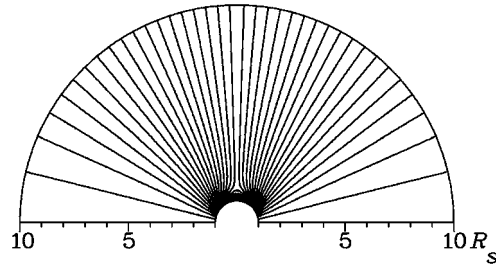


Figure 1. The initial magnetic field with a Y-type neutral point at $1.6 R_s$. The field strength at the pole on the solar surface is 4.0 G.

spatial gradients near the Sun, where it is of the order of the density scale height. A denser mesh is necessary but more computer-time consuming.

The boundary conditions are specified as follows. At the base of sub-domain I, the number density and temperature are set to be $1 \times 10^8 \text{ cm}^{-3}$ and $1 \times 10^6 \text{ K}$ between 0° and 60° , and $2 \times 10^8 \text{ cm}^{-3}$ and $1.6 \times 10^6 \text{ K}$ between 62° and 90° . The wave pressure equals $7.5 \times 10^{-4} \text{ dyn cm}^{-2}$ between 0° and 57° , equivalent to $\langle \delta v^2 \rangle^{1/2} = 30 \text{ km s}^{-1}$, and vanishes between 60° and 90° . In addition, v_θ is set to be zero, and v_r is evaluated by equivalent extrapolation of the mass flux. The conditions at the base of sub-domain II are obtained from the solution in sub-domain I. As for the top boundary of the two sub-domains, all quantities are determined by linear extrapolation. Finally, symmetrical boundary conditions are used for the equator and the polar axis.

The initial magnetic field is a partially open potential field with a neutral electric current sheet at the equator and a Y-type neutral point at $r = 1.6 R_s$ (cf., Low, 1986), as shown in Figure 1.

The magnetic field strength at the polar coronal base is taken to be 4.0 G. Figure 2 shows the initial latitudinal profiles of (a) density, (b) radial velocity, (c) temperature ($T_e = T_p$), and (e) wave pressure at several separate radial distances in sub-domain I.

Under the initial and boundary conditions prescribed above, Equations (2)–(8) are solved by the multi-step implicit scheme developed by Hu (1989) until a steady state is reached. The initial state chosen above is somewhat arbitrary but immaterial, because the final steady state only depends on the boundary conditions at the coronal base, as demonstrated by numerical simulations. In what follows, we present and discuss the numerical results.

3. Numerical Results

The present model generates the following parameters at 1 AU: $n = 2.37 \text{ cm}^{-3}$, $v_r = 770 \text{ km s}^{-1}$, $T_p = 2.96 \times 10^5 \text{ K}$, $\langle \delta B^2 \rangle / B^2 = 0.8$ for the fast solar wind, and $n = 15.7 \text{ cm}^{-3}$, $v_r = 331 \text{ km s}^{-1}$, $T_p = 5.36 \times 10^4 \text{ K}$ for the slow solar

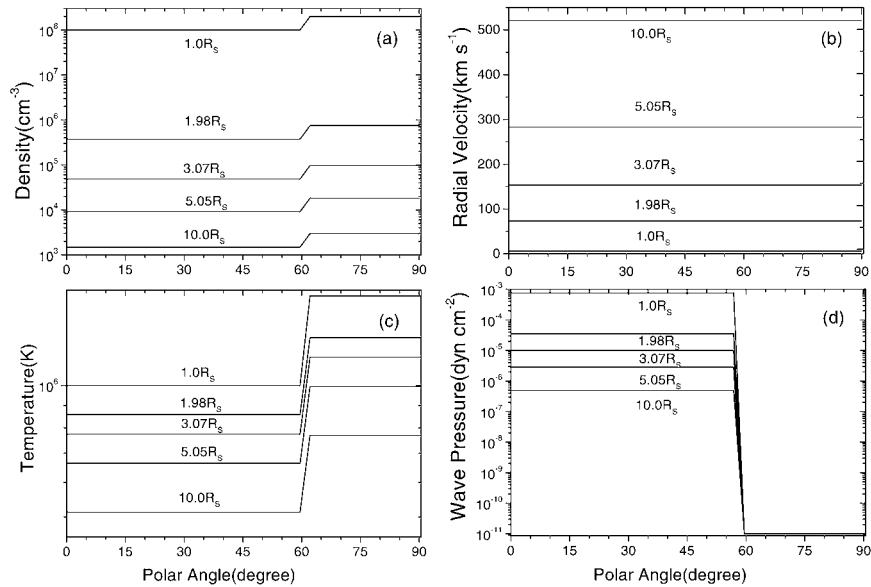


Figure 2. Density, radial velocity, temperature, flow speed and Alfvén wave pressure taken for the initial state. The electron and proton temperatures are assumed to be equal.

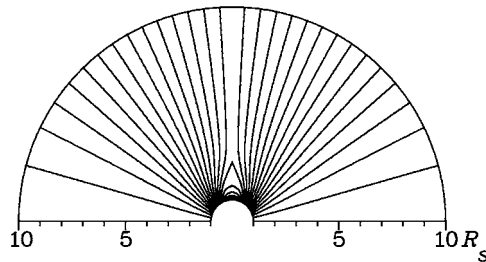


Figure 3. Topology of the steady-state magnetic field in the meridional plane for the Alfvén wave-driven solar wind model, showing a cusped streamer and a thin current sheet above it along the equator. The height of the streamer is about $2 R_s$.

wind, which essentially agree with observations (Schwenn, 1991; Villante and Vellante, 1982), except that the number density and the proton mass flux for the slow wind are slightly higher than observed. Nevertheless, such a discrepancy may be reduced through suitably adjusting the dissipation rate Q and will not affect the main conclusions to be reached below.

Figure 3 shows the magnetic configuration of the final steady state: a coronal streamer with its top at about $3 R_s$ and a narrow current sheet above it. Such a configuration is consistent with that estimated by Koutchmy and Lovshits (1993) and calculated by Steinolfson (1988), Suess *et al.* (1999), and Suess, Wang, and Wu (1996).

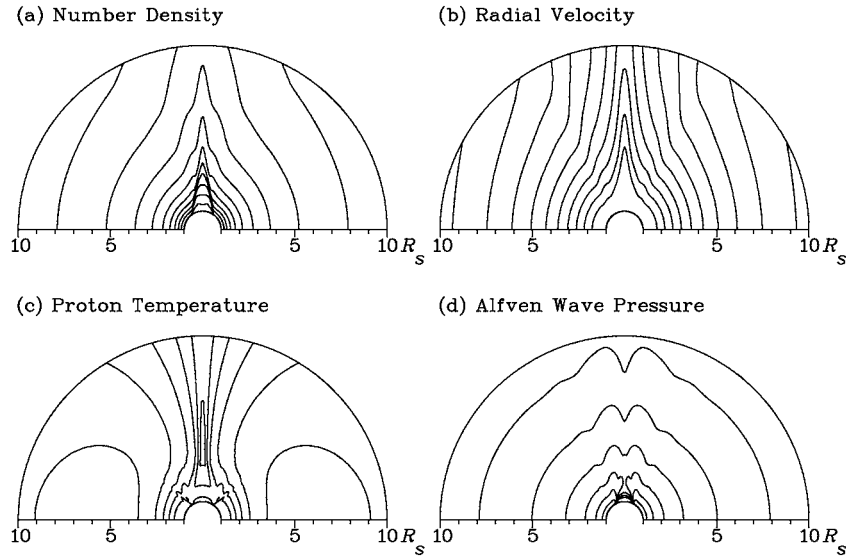


Figure 4. Contours of the number density, the radial velocity, the proton temperature, and the Alfvén wave pressure, in the unit of cm^{-3} , km s^{-1} , kelvin degree, dyn cm^{-2} , respectively. The contour level of the number density ranges from $\log_{10} n = 3$ near the top of the polar region to 8 near the streamer base, and increments by 0.5. The contour level of the radial velocity ranges from 50 to 500, and increments by 50. The contour level of the proton temperature ranges from $\log_{10} T_p = 5.95$ in the streamer region to 6.45 in the polar region, and increments by 0.1. The contour level of the Alfvén wave pressure ranges from $\log_{10} p_w = -6$ near the top to -2.5 near the pole, and increments by 0.5.

The contours of (a) number density, (b) radial velocity, (c) proton temperature, and (d) Alfvén-wave pressure in sub-domain I are shown in Figure 4. The fast solar wind appears between 0° and 60° , the slow wind between 80° and 90° , and a transition region between 60° and 80° (Figure 4(b)). In the fast wind region, the protons reach the flow speed of 520 km s^{-1} at $10 R_s$ (Figure 4(b)), and to a maximum temperature of $3 \times 10^6 \text{ K}$ at about $5 R_s$. The Alfvén-wave pressure is almost uniform in the fast wind region, but has a local maximum near the equator. This stems from a weaker magnetic field and a higher density in the slow wind region, which leads to a lower dissipation of the Alfvén waves than that in the fast wind region. On the other hand, a local minimum right at the equator is mainly attributed to a propagation effect: the Alfvén waves near the equator come from the coronal base in the open field region next to the coronal streamer and the corresponding flow tubes undergo a larger expansion which speeds up the damping of the Alfvén waves along these tubes. Nevertheless, the wave pressure remains finite throughout the slow wind region, and almost equals that in the fast wind. Such a feature is roughly preserved out to 1 AU (see Figure 5(d)).

Figure 5 gives the radial profiles of (a) number density, (b) radial velocity, (c) proton temperature, and (d) Alfvén-wave pressure from $1 R_s$ to 1 AU at several

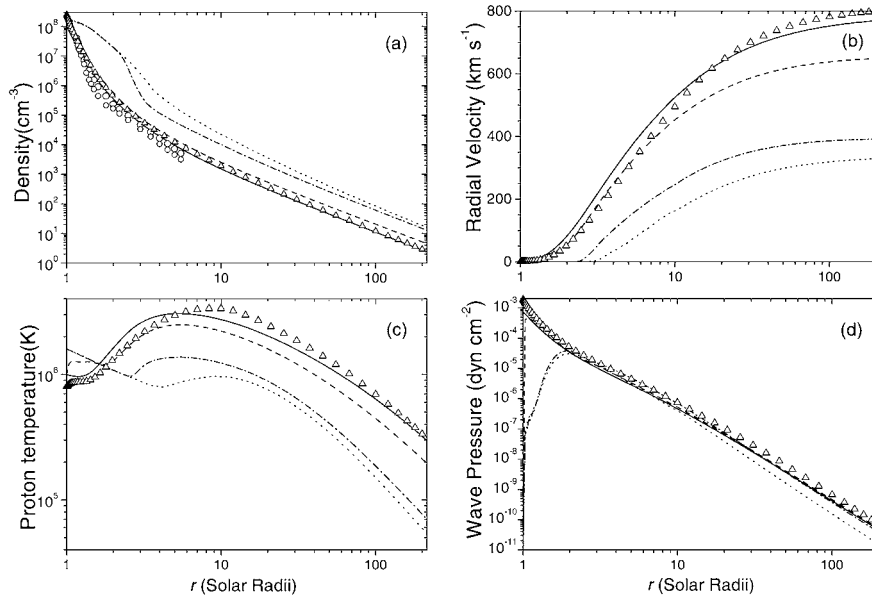


Figure 5. Radial profiles of density (a), velocity (b), proton temperature (c), and wave pressure (d) at $\theta = 3^\circ$ (solid), $\theta = 60^\circ$ (dashed), $\theta = 85^\circ$ (dot-dashed), and $\theta = 90^\circ$ (dotted) respectively. The open circles in (a) correspond to the upper and lower limits of density inferred from white-light coronagraph observations (Fisher and Guhathakurta, 1994). The corresponding profiles obtained by Hu, Habbal, and Wang (1999b) in terms of a one-dimensional model are shown as triangles.

separate colatitudes. The triangles represent the one-dimensional results from Paper HHL. It can be seen that the fast wind obtained in this paper nearly reproduces the results of one-dimensional flow tube simulations; the differences are attributed to different boundary conditions at the coronal base and the fact that the wave pressure equation is used in this paper to replace the wave spectrum equation adopted in Paper HHL. The open circles in Figure 5(a) denote the data of electron density given by Fisher and Guhathakurta (1994). The predicted profile is slightly higher than observed, implying an insufficient acceleration by the Alfvén waves in the inner corona, a common deficiency inherent in other wave-driven solar wind models (Esser, Holzer, and Leer, 1987; Hu, Habbal, and Wang, 1999). In the coronal helmet streamer, the plasma is static (Figure 5(b)), characterized by a high density, a high temperature below $1.8 R_s$, and a low temperature beyond compared to the fast wind, and the Alfvén wave pressure vanishes. Across the boundary of the streamer, the protons start to be accelerated and heated by the Alfvén waves, their flow velocity, density and temperature experience a marked variation with respect to colatitude. The proton temperature reaches its maximum at $5 R_s$ along the polar axis, and decreases monotonically with respect to increasing colatitude in the region beyond $1.8 R_s$ (Figure 5(c)). This is because the increase of the number density with increasing colatitude (Figure 5(a)) slows down the dissipation of the Alfvén waves. It can be seen from Figure 5(d) that up to 1 AU, the Alfvén-wave

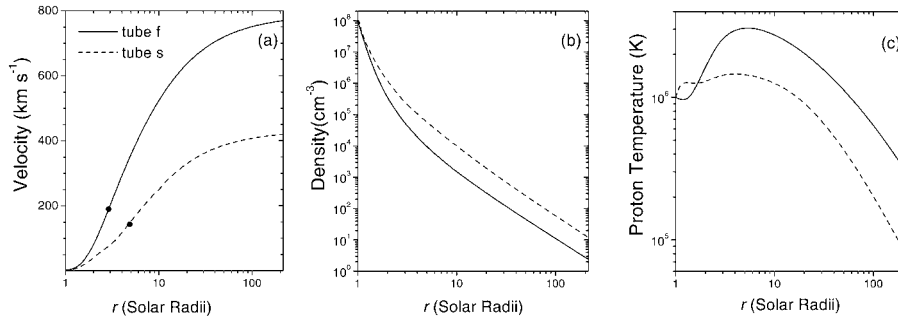


Figure 6. Radial profiles of the velocity, density and proton temperature in the two flow tubes, tube f ($\theta_o = 0^\circ$) and tube s ($\theta_o = 54^\circ$).

pressure in the equatorial region is merely slightly lower than at high latitudes which is consistent with the fact that *Helios* spacecraft observed large-amplitude Alfvén waves in slow-wind regions (Marsch *et al.*, 1981; Roberts, 1987).

In order to explore the spatial distribution of the dissipation rate of the Alfvén waves and its relation to the origin of the fast and slow winds, we single out two flow tubes (i.e., magnetic flux tubes), f and s, in the fast and slow wind regions respectively. The two tubes are footed at 0° and 54° at the coronal base in the open field region. The physical conditions are the same at the two footpoints (see Figure 2) except for the magnetic field strength. The initial magnetic field mentioned above has a similar distribution of magnetic field strength along the coronal base to that of a dipole magnetic field commonly used in two-dimensional coronal models, 4 G and 2.85 G at the footpoints of f and s tubes. As a result, the energy flux of the Alfvén waves ($= 2p_{w0}v_{A0} = B_c \langle \delta v^2 \rangle (\rho/4\pi)^{1/2}$) are 1.31×10^5 and 0.93×10^5 erg cm $^{-2}$ s $^{-1}$, respectively. After normalization to 1 AU, the magnetic field strength at the coronal base, B_c , should be replaced by B_E , the magnetic field strength at 1 AU (see Paper HHL), and the normalized wave energy flux thus obtained is 1.38 erg cm $^{-2}$ s $^{-1}$ for tube f and 1.05 erg cm $^{-2}$ s $^{-1}$ for tube s, which determine the energy budget, i.e., the acceleration and heating of the solar wind plasma in the two flow tubes. The wave energy fluxes at $10 R_s$, normalized to 1 AU, are found to be 0.34 erg cm $^{-2}$ s $^{-1}$ for tube f and 0.22 erg cm $^{-2}$ s $^{-1}$ for tube s, implying that about 80% of the wave energy is exhausted within $10 R_s$, namely, the acceleration and heating of the solar wind by the Alfvén waves occur mainly in the near-Sun region for both the fast and the slow winds.

However, the solar wind properties are remarkably different in the two flow tubes under the same coronal conditions and similar wave energy fluxes as mentioned above. Figure 6 shows the radial profiles of (a) flow velocity, (b) number density, and (c) proton temperature along tubes f and s respectively, and the solid circles in Figure 6(a) denote the critical points, $2.9 R_s$ with the sound speed 180 km s $^{-1}$ for tube f, and $4.9 R_s$ with the sound speed 143 km s $^{-1}$ for tube s. As seen from Figure 6, the flow velocity and the proton temperature are lower and the

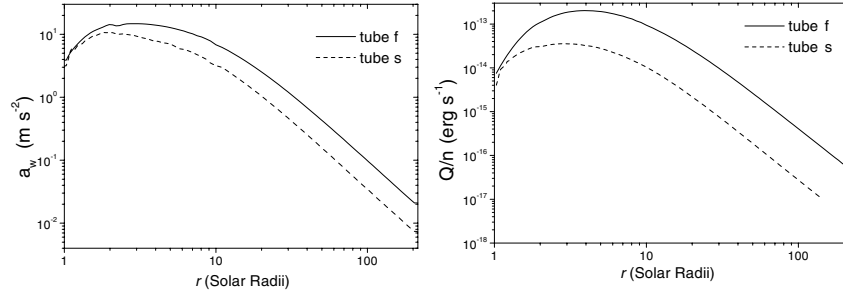


Figure 7. The acceleration and heating rate per proton provided by Alfvén waves versus r in the two flow tubes.

density is higher in tube s than those in tube f. Such differences are associated with the acceleration and heating rate per proton provided by the Alfvén waves, given by

$$a_w = -\frac{1}{\rho} \frac{\partial p_w}{\partial l}, \quad \frac{Q}{n} = \frac{2m_p}{L_{c0}} \sqrt{\frac{2B}{B_{c0}}} \left(\frac{p_w}{\rho} \right)^{3/2}, \quad (11)$$

where l is the arc length of the tube. Figure 7 shows the distribution of a_w and Q/n along tubes f and s. Owing to the closeness of the wave energy flux, a lower a_w and Q/n are mainly attributed to a higher density in tube s. Moreover, the wave dissipation rate is proportional to $B^{1/2}$. Tube s is close to the Y-type neutral point, the magnetic field in it is weaker on the whole than in tube f, leading to a further decrease of the heating rate per proton. As far as the distribution of the acceleration and the heating rate per proton is concerned, the peaks are located at $4.0 R_s$ and $3.0 R_s$, respectively for tube f, outside the corresponding critical point, and $3.0 R_s$ and $2.1 R_s$, respectively for tube s, inside the corresponding critical point. As pointed out by Leer and Holzer (1980), an input of momentum and energy in the supersonic flow region leads to an increase of the solar wind velocity and a decrease of the proton flux at 1 AU. On the contrary, the wind velocity will decrease and the proton flux will increase at 1 AU if momentum and energy are added in the sub-sonic flow region. This conclusion is consistent with the numerical results described above. Then, how is the specific spatial distribution in tubes f and s formed for the acceleration and heating rate provided by the Alfvén waves?

To answer this question, let us take a look at the different geometries of the two flow tubes. Tube f is along the polar axis, and the magnetic field strength drops monotonically with increasing heliocentric distance so that its expansion factor increases with the radial distance and eventually approaches to a constant larger than unity. Kopp and Holzer (1976) introduced the following expansion factor:

$$f(r) = \frac{f_m e^{(r-r_1)/\sigma} + 1 - (f_m - 1)e^{(R_s-r_1)/\sigma}}{e^{(r-r_1)/\sigma} + 1}, \quad (12)$$

where f_m , r_1 and σ are adjustable constants, and f_m is the maximum expansion factor. Such a flow-tube geometry has been extensively used in one-dimensional flow

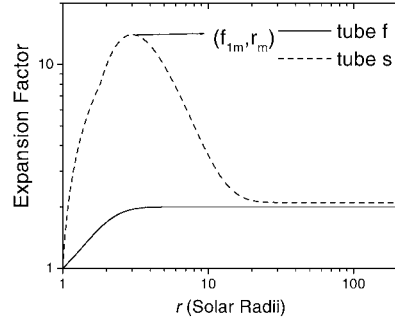


Figure 8. The cross-section expansion factor of the fast-flow tube f and the slow-flow tube s versus r given by $f(r)$ and $f_1(r)$ (see Equations (12) and (13), respectively).

tube models for the fast solar wind. In comparison with tube f, tube s passes through the neighborhood of the Y-type neutral point, where the magnetic field is weak. Therefore, the magnetic field strength undergoes a process of drop, growth, and a drop again, the corresponding expansion factor will take a maximum somewhere near the Y-type neutral point. According to the numerical results of Usmanov *et al.* (2000, cf., Figure 13 of that paper), the expansion factor for slow wind tubes increases sharply at the beginning, and then decreases monotonically after it passes through a maximum in the vicinity of the Y-type neutral point. To analyze the effect of the flow tube geometry on the solar wind properties, Equation (12) is used to describe the fast-wind flow tube, taking $f_m = 2$, $r_1 = 1.31 R_s$, and $\sigma = 0.51 R_s$, whereas for the slow-wind flow tube we construct the following expansion factor:

$$f_1(r) = \begin{cases} a_1 + a_2 [1 - e^{-(r-R_s)/a_3}]^3 e^{-(r-R_s)/a_4}, & r \geq r_2, \\ 1 + \frac{\ln(r/R_s)}{\ln(r_2/R_s)} [f_1(r_2) - 1], & r < r_2, \end{cases} \quad (13)$$

where $r_2 = 1.8 R_s$, $a_1 = 2.1$, $a_2 = 30$, $a_3 = 0.8 R_s$, and $a_4 = 3.0 R_s$. The expansion factor increases from the coronal base, reaches its maximum $f_{1m} = 14$ at $r_m = 3 R_s$, and then decreases monotonically, approaching a constant of 2.1. In addition, the slow wind flow tube is assumed to be along the radial direction to simplify the numerical calculations made below. The radial profiles of $f(r)$ and $f_1(r)$ are depicted in Figure 8.

The one-dimensional solar-wind-flow equations and Alfvén-wave-pressure equation for the two flow tubes may be derived from Equations (2), (3), and (5)–(8) by taking $\partial/\partial\theta = 0$ and inserting the flow tube geometry described by Equation (12) or (13). These equations are then solved by the time-dependent method proposed by Hu, Habbal, and Wang (1997). The boundary conditions at the coronal base are the same as those at the pole of the two-dimensional case. The steady solar wind solution obtained for the expansion factors described by Equations (12) and (13) associated with tubes f and s are shown in Figure 9 by solid and dashed curves,

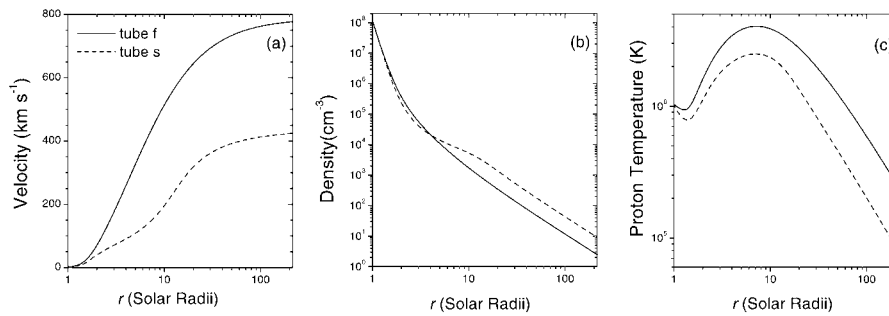


Figure 9. Radial profiles of the velocity, density, and proton temperature in tube f and tube s whose expansion factors are given in Figure 8.

respectively. These profiles turn out to be similar to their counterparts in Figure 6. The two sets of solutions are very close to each other for tube f throughout the whole domain and for tube s as well in the region beyond $10 R_s$. An appreciable difference appears within $10 R_s$ between the two sets of profiles for tube s. The reason may be twofold. First, a larger magnetic field strength was set at the coronal base in the 1-D calculation, which leads to a larger Alfvén-wave energy flux. Secondly, the geometry of tube s has not been well resolved by the present 2-D simulation because the grid spacing is too large. If these factors were properly taken into account, the 1-D model should essentially reflect the 2-D simulation results for the slow wind. Therefore, we argue that the 2-D and 1-D models may give essentially the same results in any case.

It can be seen from Figure 9 that under the same coronal base conditions, the solution corresponding to the expansion factor $f(r)$ is a fast solar wind, whereas that corresponding to $f_1(r)$ is a slow wind. There is another factor, the magnetic field strength at the coronal base, which determines the Alfvén-wave energy flux at the base and might influence the solar wind behavior along a one-dimensional flow tube. In the preceding calculations, the magnetic field strength is taken to be 4 G for both tubes, but as mentioned above, it is 2.85 G for tube s. A similar calculation was carried out for tube f described by Equation (12) and associated with a magnetic field strength of 2.85 G at the coronal base, and it turned out that the solar wind velocity obtained at 1 AU still exceeds 650 km s^{-1} . This means that the effect of the amplitude of the magnetic field strength at the base is small compared to that of the flow tube geometry. In summary, the geometry of expansion–contraction–re-expansion inherent in the slow wind flow tube plays a decisive role in generating the slow solar wind properties characterized by a low proton temperature and velocity and a high proton flux. Here we have only given one numerical example for each flow tube geometry, and a more detailed parameter study is relegated to future work.

4. Concluding Remarks

This paper makes the following improvements of the work by Usmanov *et al.* (2000): (1) to adopt the Alfvén waves as the unique energy source, and (2) to use the Kolmogorov rate as the dissipation rate for the Alfvén waves. The two-dimensional Alfvén-wave-driven solar wind model thus obtained in the meridional plane gives a coronal structure which is reasonable and essentially agrees with observations. The chief conclusions are summarized as follows: (1) the acceleration and heating by the Alfvén waves occur mainly in the near Sun region, (2) the flow tube geometry is a decisive factor for the formation of the slow solar wind, and (3) the 2-D and 1-D models give essentially the same results for both the fast and the slow winds.

Since the acceleration and heating of the solar wind plasma by Alfvén waves take place mainly in the near Sun region, it is hard to assess the validity of the Alfvén-wave driving mechanism based on present observations which have been limited to regions beyond 0.3 AU. The fact that Alfvén waves were observed both in the fast wind and in the slow wind and that sometimes the slow wind shows purer Alfvénic fluctuations than the fast wind does indicates that Alfvén fluctuations are essentially independent of the solar wind velocity. This was taken as one adverse evidence against Alfvén-wave-driven solar wind models (e.g., Roberts, 1996). However, this study demonstrates that the existence of Alfvén waves in the slow wind does not deny the wave-driven solar wind model, and that the effect of Alfvén waves on the acceleration and heating of the solar wind depends on the flow tube geometry. Flow tubes in the fast and slow wind regions have different geometries that determine the spatial distribution of the momentum and heat deposition of the Alfvén waves. As a result, either a fast or a slow wind may be generated by Alfvén waves under almost the same coronal base conditions, as illustrated above by numerical examples. In light of the remarkable difference between the fast and slow wind properties, it was suggested that the slow wind may have different sources on the Sun and different acceleration and heating mechanisms in the corona (e.g., Gosling, 1996). Although the present simple model cannot explain the details of the slow wind, including its high variability (Feldman *et al.*, 1977), our model describes the general properties of the slow wind in the presence of Alfvén waves. In other words, from a theoretical point of view Alfvén waves may be taken as an efficient mechanism for both the fast and slow winds.

In the present model the Alfvén waves are described only by the wave pressure, and the dissipation rate does not depend on the wave spectrum. A more rigorous approach is to simultaneously solve the solar wind-flow equations and the wave-spectrum equation, as taken by Paper HHL. Such a formidable task awaits efficient numerical methods.

Acknowledgements

The author Y. C. is grateful to Mr W. Liu of Stanford University for valuable discussions. The work was supported by the National Natural Science Foundation of China under grant 49974035 and the Innovation Engineering Fund of the USTC.

References

- Braginskii, S.I.: 1965, in M. A. Leontovich (ed.), 'Transport Processes in a Plasma', *Reviews of Plasma Physics*, Vol. 1, Consultants Bureau, New York, p. 205.
- Esser, R., Holzer, T. E., and Leer, E.: 1987, *J. Geophys. Res.* **92**, 13377.
- Feldman, W. C., Asbridge, J. R., Bame, S. J., and Gosling, J. T.: 1977, in O. R. White (ed.), *The Solar Output and its Variation*, Colorado Assoc. Univ. Press, Boulder, p. 351.
- Fisher, R. R. and Guhathakurta, M.: 1994, *Space Sci. Rev.* **70**, 267.
- Gosling, J. T.: 1996, in S. R. Habbal (ed.), *Robotic Exploration Close to the Sun: Scientific Basis*, AIP, New York, p. 23.
- Hartle, R. E. and Sturrock, P. A.: 1968, *Astrophys. J.* **151**, 1155.
- Hollweg, J. V.: 1986, *J. Geophys. Res.* **91**, 4111.
- Hollweg, J. V. and Johnson, W.: 1988, *J. Geophys. Res.* **93**, 9457.
- Hu, Y. Q.: 1989, *J. Comput. Phys.* **84**, 441.
- Hu, Y. Q. and Habbal, S. R.: 1999, *J. Geophys. Res.* **104**, 17045.
- Hu, Y. Q., Esser, R., and Habbal, S. R.: 1997, *J. Geophys. Res.* **102**, 14661.
- Hu, Y. Q., Esser, R., and Habbal, S. R.: 2000, *J. Geophys. Res.* **105**, 5093.
- Hu, Y. Q., Habbal, S. R., and Li, X.: 1999, *J. Geophys. Res.* **104**, 24819 (Paper HHL).
- Kopp, R. A. and Holzer, T. E.: 1976, *Solar Phys.* **49**, 43.
- Koutchmy, S. and Lovshits, M.: 1992, *Space Sci. Rev.* **61**, 393.
- Leer, E. and Holzer, T. E.: 1980, *J. Geophys. Res.* **85**, 4681.
- Low, B. C.: 1986, *Astrophys. J.* **310**, 953.
- Marsch, E., Muhlhauser, K.-H., Rosenbauer, H., Schwenn, R., and Denskat, K. U.: 1981, *J. Geophys. Res.* **86**, 9199.
- Pneuman, G. W. and Kopp, R. A.: 1971, *Solar Phys.* **18**, 258.
- Roberts, D. A.: 1996, in S. R. Habbal (ed.), *Robotic Exploration Close to the Sun: Scientific Basis*, AIP, New York, p. 185.
- Roberts, D. A., Goldstein, M. L., Klein, L. W., and Matthaeus, W. H.: 1987, *J. Geophys. Res.* **92**, 12023.
- Schwenn, R.: 1991, in Schwenn, R. and Marsh, E., (eds.), *Physics of the Inner Heliosphere. 1. Large-Scale Phenomena*, Springer-Verlag, New York, p. 99.
- Spitzer, L., Jr.: 1962, *Physics of Fully Ionized Gases*, Wiley-Interscience, New York.
- Steinolfson, R. S.: 1988, *J. Geophys. Res.* **93**, 14261.
- Steinolfson, R. S., Suess, S. T., and Wu, S. T.: 1982, *Astrophys. J.* **255**, 730.
- Suess, S. T., Wang, A.-H., and Wu, S. T.: 1996, *J. Geophys. Res.* **101**, 19957.
- Suess, S. T., Wang, A.-H., Wu, S. T., Poletto, G., and McComas, D. J.: 1999, *J. Geophys. Res.* **104**, 4697.
- Tu, C. -Y.: 1987, *Solar Phys.* **109**, 149.
- Tu, C. -Y.: 1988, *J. Geophys. Res.* **93**, 7.
- Tu, C.-Y., Pu, Z. Y., and Wei, F. S.: 1984, *J. Geophys. Res.* **89**, 2521.
- Usmanov, A. V., Goldstein, M. L., Besser, B. P., and Fritzer, J. M.: 2000, *J. Geophys. Res.* **105**, 12675.
- Villante, U. and Vellante M.: 1982, *Solar Phys.* **81**, 367.
- Wang, A.-H., Wu, S. T., Suess, S. T., and Poletto, G.: 1993, *Solar Phys.* **147**, 55.